

Emergence of central recirculation zone in a V-shaped premixed swirling flame

Qiuxiao Wang, Yongzhi Ren, Mingming Gu, Bowen Yu, Xiaoxing Feng, Fei Qi, Xi Xia*

School of Mechanical Engineering, Shanghai Jiao Tong University,

Shanghai 200240, P. R. China

* Corresponding author

E-mail address: xiaxis@sjtu.edu.cn (Xi Xia)

Abstract

This paper presents an experimental study on the emergence of the central recirculation zone (CRZ) in a V-shaped premixed swirling flame, using simultaneous measurement of particle image velocimetry (PIV) and CH* chemiluminescence. The results show that either increasing the Reynolds number (Re) or decreasing the equivalence ratio (Φ) would facilitate the emergence of CRZ, and the inner shear layer (ISL) plays an essential role in governing the characteristics of CRZ. Further analysis demonstrates that the CRZ emergence can be promoted by higher ISL intensity but suppressed by enhanced viscous diffusion owing to higher flame temperature. As such, the CRZ formation can be interpreted as the outcome of a competition between the ISL intensity, i.e., circulation, and the vorticity consumption due to viscous diffusion. This competition physically corresponds to a special Reynolds number, Re_s , defined as the ratio between the ISL circulation (Γ) and the ISL effective viscosity (ν_s), with a simplified heat loss model proposed for the temperature and viscosity estimations of the ISL. The outputting $\Gamma - \nu_s$ plot yields a single boundary line separating the cases with and without CRZ, which points to a common critical Re_s of about 637, justifying the generality of the present criterion for lean-premixed V-shaped swirling flames of various operating conditions. Unlike most previous works which study the CRZ of a swirling flame from the point of vortex breakdown, the present work reveals the importance of enhanced viscous diffusion, caused by flame heating, in suppressing the CRZ emergence.

I. INTRODUCTION

Swirl combustion is prevalently adopted in power and propulsion systems, such as gas turbines and aero-engines [1-3]. The essence of applying swirl in combustion is to create a central recirculation zone (CRZ) [4], where the temperature is sufficiently high to serve as a continuous ignition source and the flow speed is sufficiently low to be matched with the flame speed, thereby promoting flame anchoring and stabilization [5]. Moreover, the CRZ in a sense is similar to a stirred reactor that produces nearly uniform distributions of reactant-product mixture and temperature, which help to improve combustion efficiency and reduce emission [6].

Essentially, the swirl-induced CRZ is a fluid dynamical phenomenon resulting from vortex breakdown [5,7]. It occurs as a strong swirling vortex tube suddenly expands and ruptures into a cone or bubble, inside of which flow reverses to form a recirculation zone [8]. The basic characteristics of CRZ in swirling flows have been extensively studied [5,9,10]. Syred and Beer [5] experimentally found that the width of the CRZ increases with the swirl number, while the length of the CRZ first increases and then decreases with the swirl number. They also found that a divergent exit nozzle can create a larger CRZ and substantially reduce the threshold swirl number to trigger the onset of CRZ. Wang *et al.* [10] reported that the width and length both increase with the Reynold number (Re). Nogenmyr *et al.* [9] concluded that the existence of confinement could significantly enlarge the CRZ.

In swirling flames, the formation mechanism and characteristics of CRZ should be largely consistent with those for the non-reacting flow case. However, the behaviors of CRZ can be substantially affected by combustion through two main mechanisms. One is associated with the heat release process, which causes thermal expansion of burned gases and results in significantly accelerated flow downstream of the flame front; the other is related to the aftermath of heat release,

i.e., the increased gas temperature, which influences the fluid dynamics through changed fluid properties, such as density and viscosity. For example, Gouldin *et al.* [11] experimentally studied the flow characteristics in a swirl combustor and found that combustion can promote the onset of vortex breakdown. Choi *et al.* [12] numerically found that the critical swirl number for the emergence of CRZ first decreases and then increases as the exothermicity is increased. Umeh *et al.* [13] experimentally studied the effects of equivalence ratio (Φ) on CRZ in swirling flames and found that the CRZ reduces and its position moves downstream with increasing Φ . Wang *et al.* [14,15] recently found that the length of CRZ in single swirling flames is shorter compared with the cold flow, but it could increase in the case of stratified swirling flames. They also observed spiral-shaped CRZ in stratified swirling flames and found that the outer main flame has a marginal influence on the CRZ compared with the inner pilot flame [16].

Albeit numerous research has been conducted, an in-depth and consistent understanding of the formation and characteristics of CRZ in basic swirling flames remains out of reach. This is probably because most relevant studies were conducted based on engineering-derived combustors [13,17], which usually involve complex structures for the inner duct and nozzle. For example, the swirler could induce significant wake vortices, which turn the flow into turbulence even at a small Reynolds number; a divergent nozzle or a central bluff body could promote the formation of CRZ. These additional factors make it difficult to set up clean boundary conditions for a scientific problem, let alone extract the core mechanisms or draw general conclusions.

Given this background, this study is motivated by a simple question: what determines the emergence of CRZ in a general swirling flame? To this end, we first develop a novel swirl burner to generate a basic swirling flame, which is free from the influences of hetero nozzle shape, central bluff body, or turbulent wake after the swirler. Then, the CRZ characteristics of lean-premixed

methane-air swirling flames are experimentally investigated for wide ranges of Reynolds number and equivalence ratio, based on simultaneous measurement of particle image velocimetry (PIV) and flame chemiluminescence. The results enable us to identify a threshold condition based on the inner shear layer surrounding the CRZ, which sheds light on the general CRZ formation mechanism in the lean combustion regime.

II. EXPERIMENTAL METHOD

The experimental setup consists of a novel single-nozzle open-head swirl burner of methane/air premixture and a simultaneous PIV/CH* chemiluminescence diagnostic system. As shown in Fig. 1, the burner contains a radial swirler of cambered-NACA-airfoil arrays to induce a swirling flow with minimum wake. The nozzle exit has a diameter of $D = 20$ mm, and features a convergent design with a streamlined center cone to suppress the upstream flow separation. For further suppression of upstream turbulence, the premixed gas was decelerated via a divergent annular section, ensuring that the flow impinges on the swirler vanes in a low-speed laminar regime. Both fuel and air streams were regulated by mass flow controllers (SevenStar series) at 1atm and 298K. By setting the fuel and air flowrates, the operation conditions for the present experiment were adjusted in terms of the Reynolds number (Re , range: 2000~7000) and the equivalence ratio (Φ , range: 0.5~1.0). Here, $Re = UD/\nu$ is defined based on the bulk velocity (U) at the nozzle exit, the exit diameter (D), and the kinematic viscosity (ν) of the fresh mixture; $\Phi = S_{toic}m_f/m_a$ is calculated based on the stoichiometric air-to-fuel mass ratio ($S_{toic} = 17.11$ for methane/air combustion), and the mass flow rates of fuel (m_f) and air (m_a).

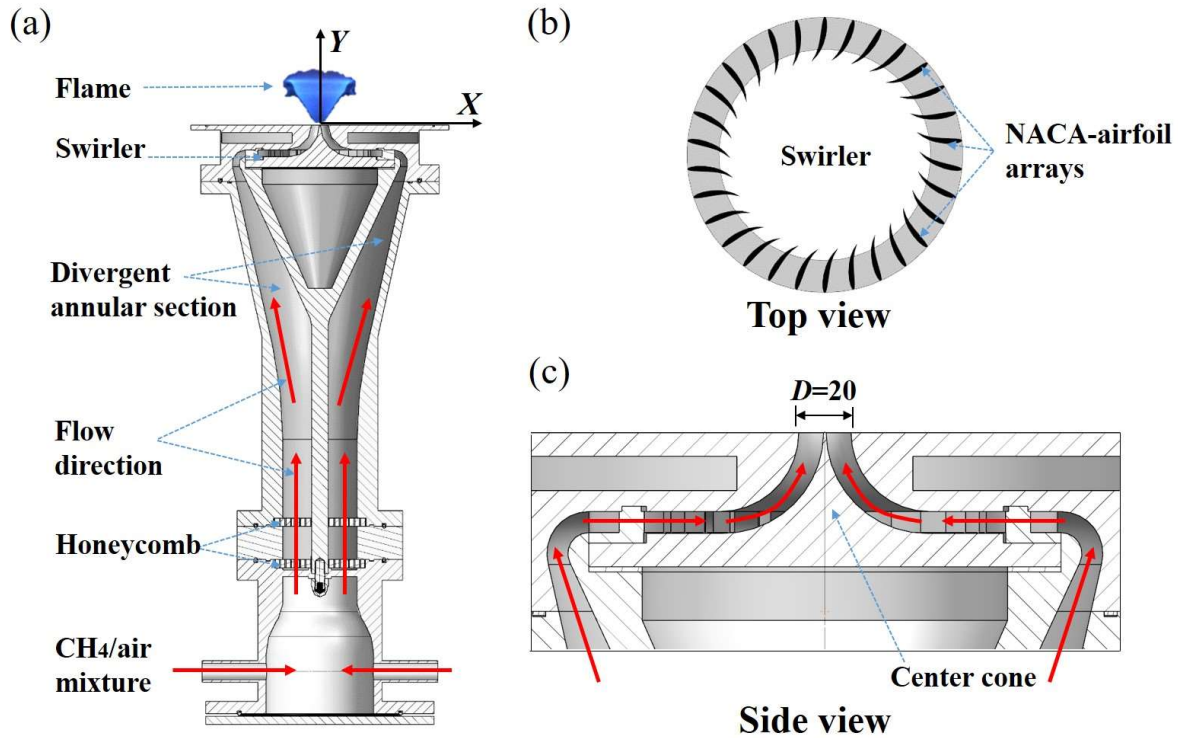


FIG. 1. Schematics of the swirl burner.

Fig. 2 presents the laser diagnostic system, the core of which is a dual-cavity Nd:YLF laser (Beamtech Vlite-Hi-527), which outputs green light of 527 nm at 3.1 mJ/pulse and a repetition rate up to 10 kHz. Two high-speed CMOS cameras (Phantom VEO1310L) with a maximum frame rate of 10.8 kHz at full resolution (1280×960 pixels) were used for PIV and chemiluminescence imaging, respectively. For PIV measurement, aluminum oxide particles of ~1 μm diameter were seeded in the air stream as flow tracers (Stokes number ~0.023). Particle images were recorded at 10,000 fps by the PIV camera with a Nikkor lens (Nikkor 50 mm f/1.4G) and a short bandpass filter (Edmund Optics 527/20 nm). The field-of-view (FOV) was about 80 mm × 60 mm with a resolution of ~62 μm /pixel. For the main study, the laser sheet was aligned with the central vertical plane of the swirling flame. To evaluate the swirl number, the laser sheet was expanded horizontally to measure the transverse velocity field at the cross-section 2 mm above the nozzle

exit. The velocity vectors were computed using a multi-scale cross-correlation PIV algorithm (LaVision Davis 8.0), with a final interrogation window size of 24×24 pixels and 50% overlap, resulting in a flow-field resolution of 0.744 mm/point. To simultaneously capture the flame structure, CH* chemiluminescence was recorded by the CH* camera attached with an intensifier (Lambert HiCATT) and a short bandpass filter (Edmund Optics, 430/10 nm).

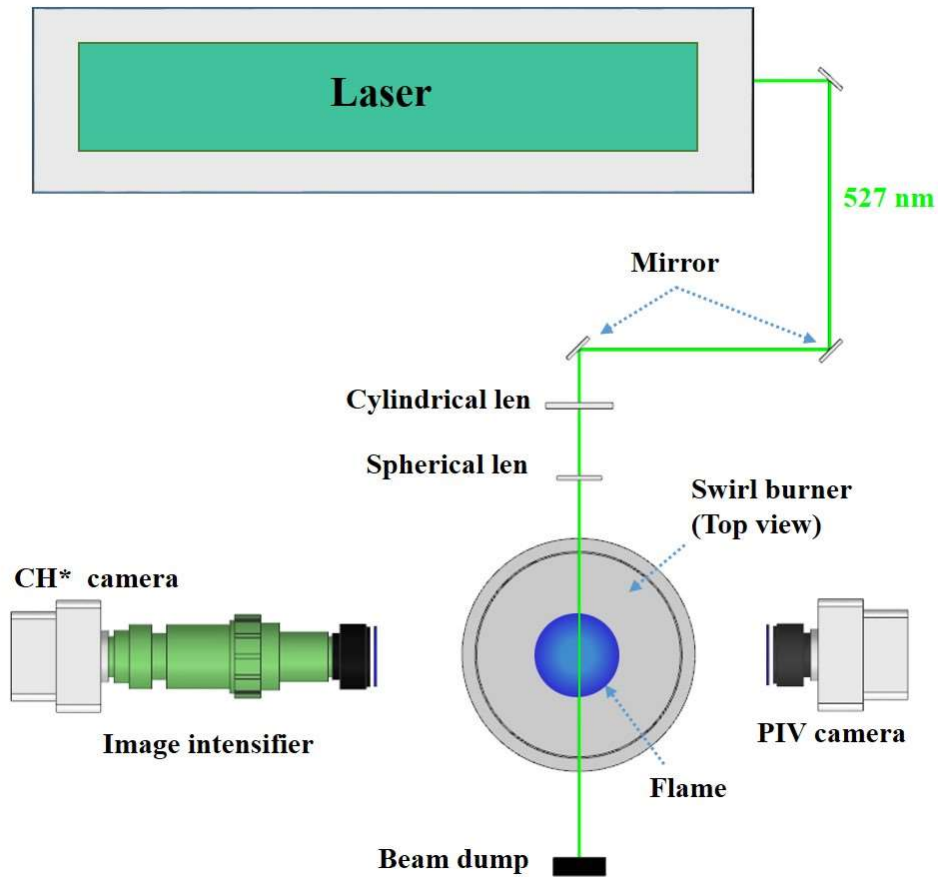


FIG. 2. Schematic of the laser diagnostic system.

III. PARAMETRIC STUDY OF CRZ EMERGENCE

A. Phenomenological description and regime nomogram

We first seek a phenomenological interpretation of the CRZ in swirling flames, based on the simultaneous PIV/CH* chemiluminescence system measurement. The flame and flow evolutions of two representative cases are presented in Fig. 3(a) and 3(b), corresponding to situations with and without CRZ, respectively. In the left half of each subplot, Abel inversion [18] of the CH* chemiluminescence signal is first performed to expose the flame front; then, the flame front is extracted and overlapped with the vorticity field and streamlines in the right-half subplot. For the lean-premixed combustion concerned in the present work, the swirling flames feature a V-shaped flame front, a weak inner shear layer (ISL), and a strong outer shear layer (OSL). The ISL decays, and its vorticity diffuses as it evolves downstream, whereas the OSL rolls up into vortex rings owing to the Kelvin–Helmholtz instability. The V-shaped flame front is anchored at the inner root of the ISL and then extends across the ISL to interact with the OSL in the far field. The coupling between the flame front roll-up and the outer vortex ring (OVR) movement confirms our previous finding [14,15] that the OVR dominates the flame dynamics and heat release rate fluctuation of a V-shaped flame. Unlike a fully turbulent flame, whose flame front is irregular and even fragmented owing to the turbulent eddies of different sizes, the flame fronts of the V-shaped swirling flames in Fig. 3 are relatively smooth, and the flame roll-up behaviors render periodic dynamics owing to the coherent OVRs developed from the OSL; these indicate that the present flow and flame starts from laminar in the near field and gradually transitions to turbulence in the downstream. A notable difference between the two cases lies in the presence of a CRZ in Fig. 3(a), which is enclosed by the ISL; however, no CRZ can be found in Fig. 3(b). Meanwhile, the flame in Fig. 3(a) lasts up to more than 40 mm downstream, whereas the flame height in Fig. 3(b) is

around 30mm. Apparently, different V-shaped flames could have different CRZ characteristics, which intrigues us to understand the formation mechanism of CRZ, especially, what determines its emergence.

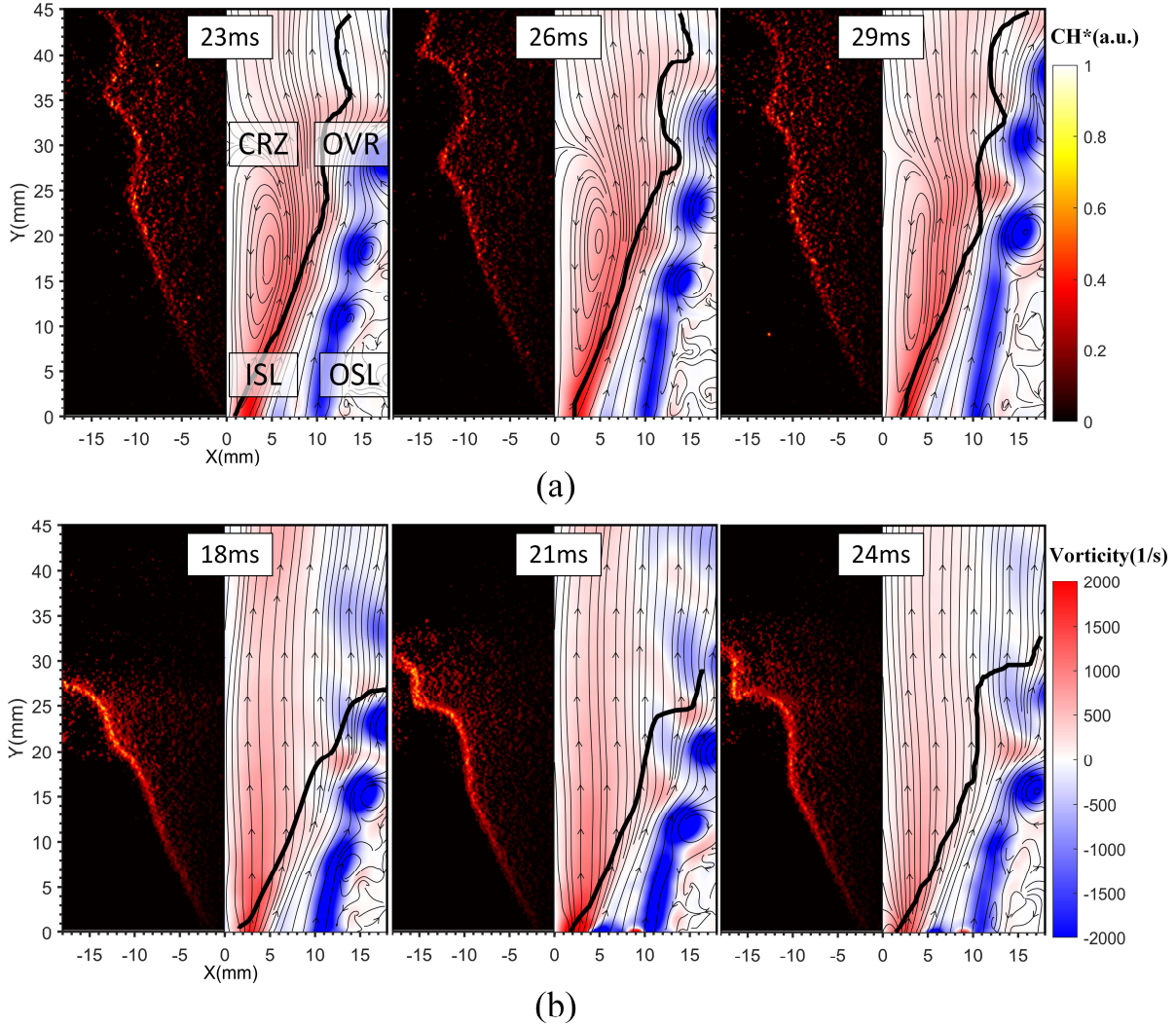


FIG. 3. The evolutions of the flame front (left) and flow field (right) for two representative V-shaped flames, (a) with CRZ at $Re = 3000$ and $\Phi = 0.56$, and (b) without CRZ at $Re = 4000$ and $\Phi = 0.8$. In each snapshot, the left-half image is the Abel inversion of the CH^* chemiluminescence field; the right-half plot shows the vorticity field overlapped by the streamlines, where the black line marks the flame front extracted based on the ridge of the CH^* intensity field.

In this work, we investigate the CRZ emergence and its influencing factors with different swirling flames obtained in a wide parameter space of Re and Φ (Re : 2000~7000, Φ : 0.5~1.0), which roughly covers the lean-premixed V-shaped flame in the laminar-to-turbulent transition regime. The parameters outside the above range were not studied as the flame could take different modes. For example, the flame could turn to M-shaped when Φ is larger than 1, and become lifted when Re is larger than 7000. The resulting $Re - \Phi$ regime nomogram is shown in Fig. 4, where the black dashed line denotes the critical boundary line between the regimes with and without CRZ. We can observe that either increasing Re or decreasing Φ could promote the emergence of the CRZ, and the critical Re increases with Φ . Moreover, the limiting behaviors of the critical line at both ends seem to indicate that there could exist a low- Φ threshold and a high- Re threshold, beyond which the CRZ would always appear. These critical conditions will be further discussed in section IV. Given the relevance of Re and Φ in dictating the fluid dynamics and chemical reaction, respectively, the formation mechanism for the CRZ can be viewed as a competition between the positive effect of jet momentum and the negative effect of the reaction rate. These effects will be explored in detail in the following section.

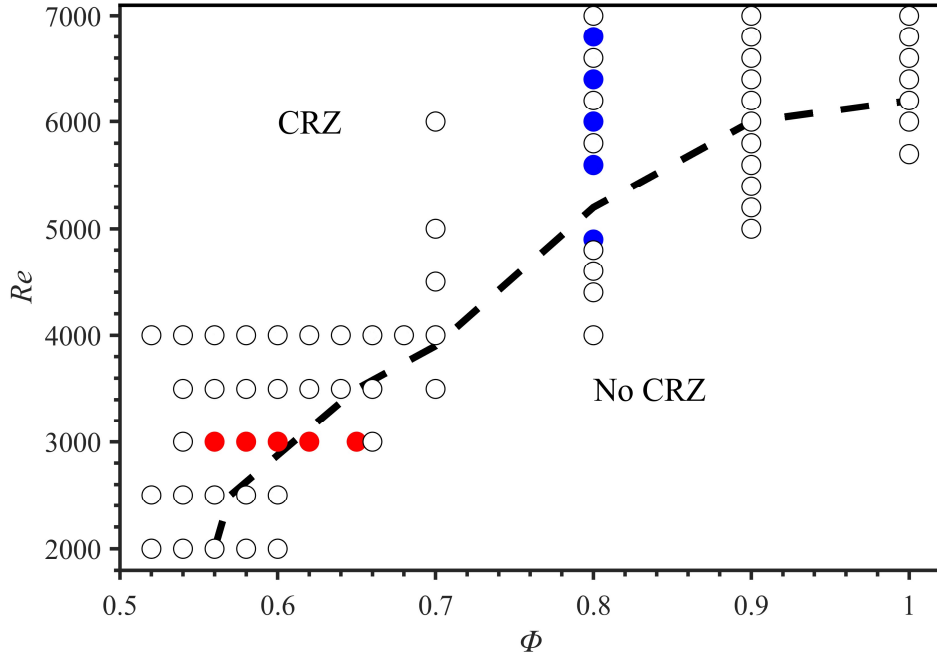


FIG. 4. Regime nomogram for CRZ emergence in the $Re - \Phi$ parameter space, based on 69 sets of experimental data. The dashed line denotes an approximate boundary between the flame regimes with and without the CRZ. The red and blue dots correspond to the cases analyzed in section III.B.

B. Effects of Re and Φ

We now separately study the effects of Re or Φ on the characteristics of CRZ by varying one parameter while fixing the other. Test runs were first carried out at various equivalence ratios (0.56, 0.58, 0.60, 0.62, and 0.65) and a fixed Re of 3000, which correspond to the cases marked by the red dots in Fig. 4. For quantitative estimation of the CRZ characteristics, the flow field and the flame front are analyzed in a time-averaged manner. In Fig. 5(a), we can readily observe that the size of the CRZ first decreases with increasing Φ and then disappears at a critical equivalence ratio of $\Phi = 0.62$. Meanwhile, the flame height also decreases with increasing Φ , owing to the larger reaction rate, which causes a faster reactant consumption than streamwise reactant transportation. To investigate how Re influences the CRZ, experiments were performed for a fixed

equivalence ratio of 0.8 and various Re (4800, 5600, 6000, 6400, 6800), which correspond to the cases marked by the blue dots in Fig. 4. It can be observed from Fig. 5(b) that the CRZ appears and then grows in size with increasing Re ; and the flame grows taller with Re owing to the higher streamwise jet velocity, which brings the reactants farther downstream within a certain reaction period.

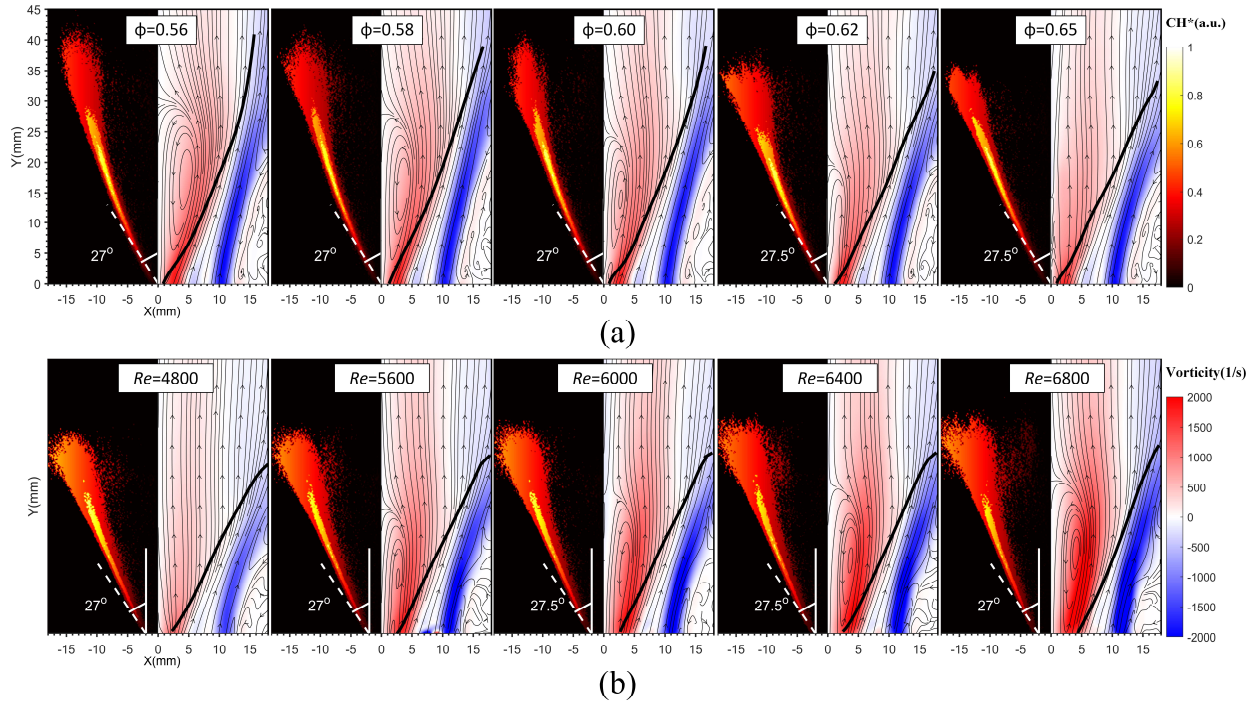


FIG.5. Comparisons of time-averaged flame front (left) and flow field (right) for (a) various equivalence ratios, $\Phi = 0.56, 0.58, 0.60, 0.62,$ and 0.65 at $Re = 3000$ and (b) various Reynolds numbers, $Re = 5100, 5600, 6000, 6400,$ and 6800 at $\Phi = 0.8$.

To quantify the above influences of Re and Φ , we first identify the boundary of the CRZ based on the zero-axial velocity contour, as shown in Fig. 6(a). Then, the geometric parameters of the CRZ, including the height (H), width (W), and area (S), can be defined accordingly in Fig. 6(b). And the total reverse momentum, M , is calculated as

$$M = \int_0^H \int_0^R (2\pi\rho v r) dr dh, \quad (1)$$

where ρ is the density of the burned gas, v is the axial velocity component, and R is the radius of the CRZ boundary at a given height h .

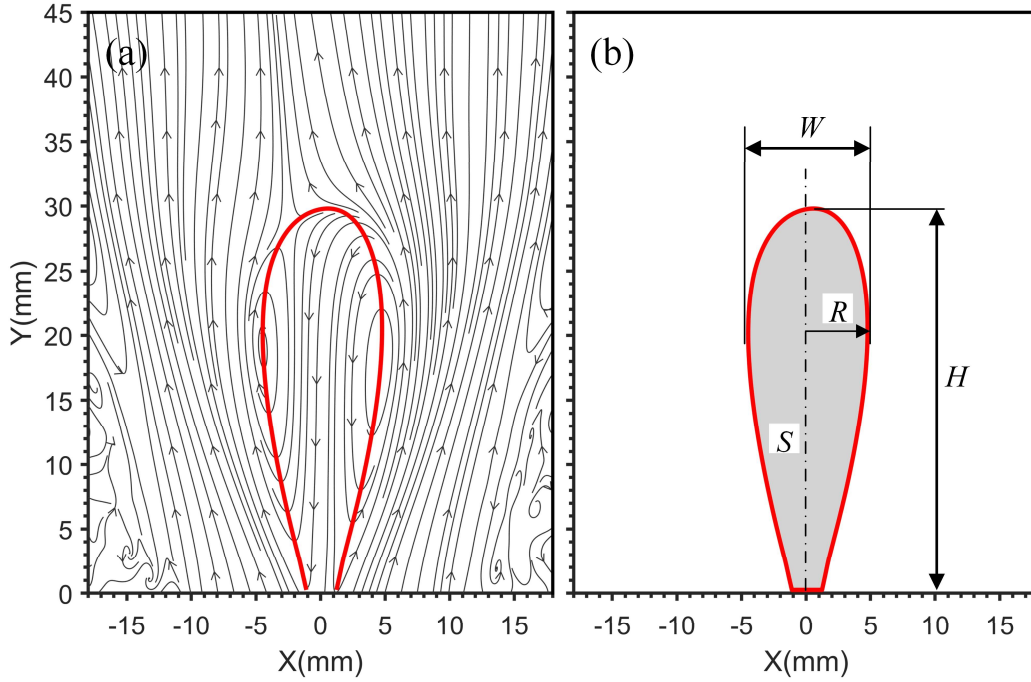


FIG.6. Definitions of height H , width W , and area S of the CRZ. The red solid line represents the boundary of the CRZ.

Fig. 7 plots the variations of H , W , S , and M as a function of Re or Φ , for various cases. In general, the variation trends of these parameters are consistent with the qualitative observations obtained by eyeballing the CRZ size in Fig. 5. We can readily observe that H , W , and S decrease with increasing Φ in Fig. 7(a)-(c), but increase with increasing Re in Fig. 7(e)-(g). In particular, Fig. 7(d) shows that M decreases and then approaches zero with increasing Φ , and Fig. 7(h) shows that M increases from zero with increasing Re . Since $M = 0$ basically means no CRZ, we propose M as a criterion to quantitatively decide the emergence of CRZ, especially for the critical cases. It

should be noted that as M approaches zero, H , W , and S still have non-zero values, some of which are even notably greater than zero. We clarify that these non-zero values in the critical cases are probably associated with artificial velocity interpolation in the PIV calculation and thus should be considered inaccurate. It happens when slight flow separation occurs at the jet centerline and forms a narrow slit type of wake void of tracer particles. In such a critical case, CRZ is unlikely to present; otherwise, particles would fill in the wake. However, interpolated velocities were still generated for the blank region in the current PIV algorithm, resulting in overestimated CRZ dimensions.

Before moving on, we note an interesting observation from Fig. 5 that a qualitative correlation exists between the size of the CRZ and the strength of its surrounding ISL. Specifically, for a smaller- Φ case in Fig. 5(a) or a higher- Re case in Fig. 5(b), the vorticity is higher, its distribution is more concentrated, and the ISL is more capable of penetrating downstream. However, the same cannot be concluded in cross-comparing the cases between Fig. 5(a) and 5(b). This indicates that the ISL could play an essential role in governing the CRZ, but its strength might not be the only factor. The exact mechanism will be further explored in section IV.

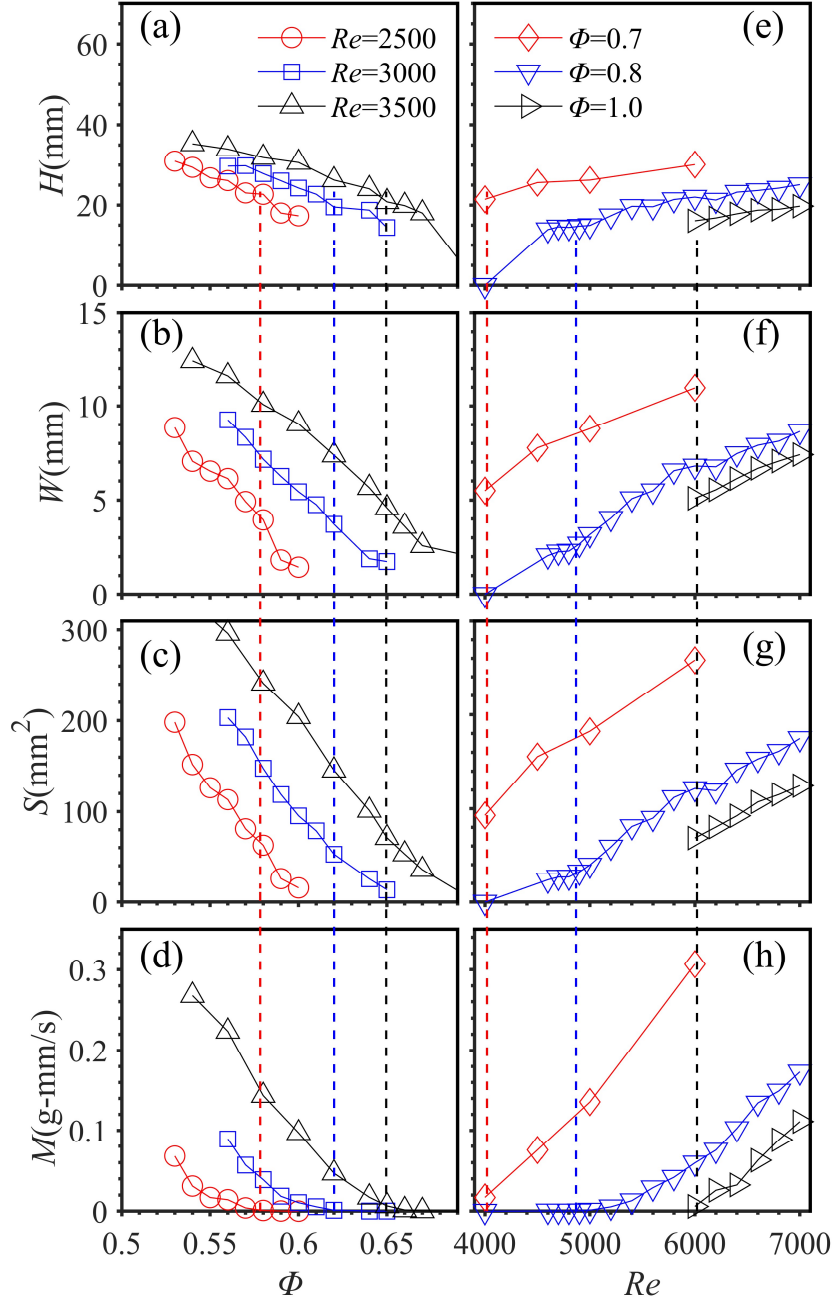


FIG. 7. Dependencies of CRZ characteristics, including height H , width W , area S , and reverse momentum M , on Φ and Re . The dashed lines mark the critical Φ and Re for the emergence of CRZ.

C. Effect of swirl intensity

Swirl intensity is another crucial factor influencing CRZ formation by means of inducing a vortex breakdown (VB) bubble [19,20], and it has a strong correlation with the flame angle at the base. Liu et al. [21] reported that the mean flame angle is mainly determined by the swirl number, with a higher swirl number corresponding to a larger flame angle. Palies et al. [22] found that the flame angle varies synchronously with the swirl number for flames under external excitations. Here, we adopted a method similar to O'Connor and Lieuwen [23] to calculate the flame angle. The results are marked in Fig. 5, showing that the flame angle maintains around 27° with slight variation, which means an almost constant swirl intensity.

To explore the relevance of swirl intensity in affecting the CRZ, the swirl intensity is quantified using the swirl number (S_N), defined as the ratio between the axial flux of tangential momentum, G_θ , and the axial momentum flux, G_x , in the form [24],

$$S_N = \frac{G_\theta}{(D/2)G_x} = \frac{2\pi\rho \int_0^\infty V_x V_\theta r^2 dr}{\pi\rho D \int_0^\infty (V_x^2 - \frac{V_\theta^2}{2}) r dr}, \quad (2)$$

where ρ is the gas density, V_x the axial velocity, V_θ the tangential velocity. Based on the transverse velocity field measured at 2 mm above the nozzle exit, we calculated S_N for the cases of $Re = 2500$, 3000, and 3500 in Fig. 4, and the results are plotted in Fig. 8. We find that for different cases S_N falls into a small range, 0.36~0.38, which accords with the above observation of the near-constant flame angles for different cases. The near-constant S_N is not surprising since only one swirler was adopted in this experiment. This result states that in the present study the change in the CRZ behaviors, including the size and shape, does not result from swirling. However, considering that the swirling effect acts on the CRZ through VB, the underlying implication is profound—the CRZ

characteristics are not just the outcome of VB but also controlled by the the thermal-fluid effects downstream of the nozzle, to which little attention has been paid in previous studies.

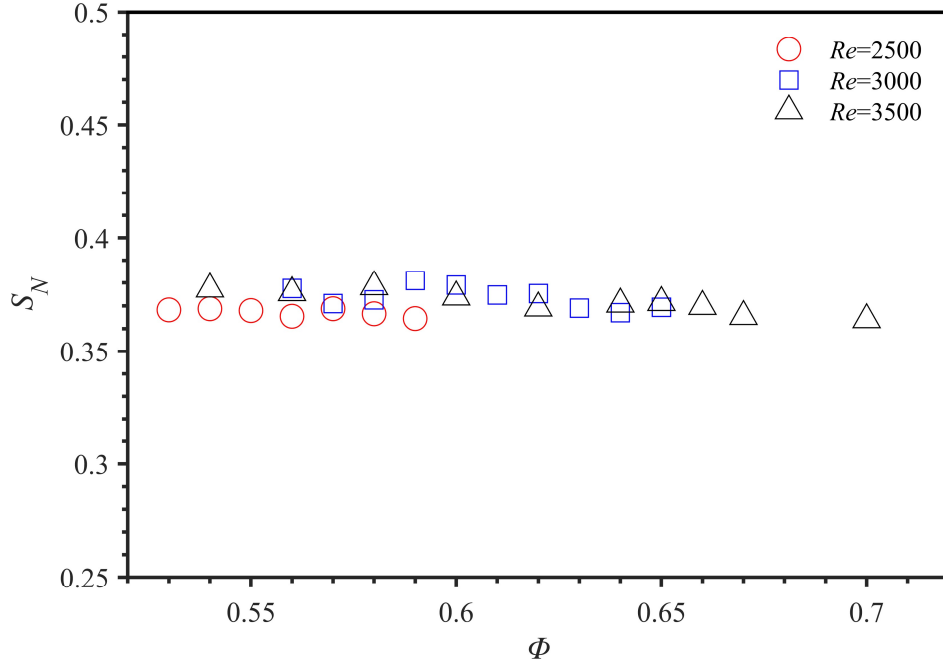


FIG.8. Variations of swirl number S_N with Φ and Re .

IV. MECHANISM GOVERNING CRZ EMERGENCE

A. Circulation of the ISL

Section III.B offers a qualitative understanding that enhanced ISL could promote the emergence or increase the size of the CRZ. This can be understood that the CRZ and the ISL are in direct contact, resulting in a coupling interaction that could strongly influence the flame and flow dynamics. Such coupling effect was also evident in Stöhr *et al.*'s experiment [25], showing that the precessing vortex core (PVC) stemmed from the ISL interacts with the CRZ and changes the flame stagnation point periodically. They also found that the OSL has no direct effect on the CRZ because they are separated from each other by the ISL. Zhang *et al.* [26] found that the coupled movements of CRZ and PVC cause the transition of the CRZ shape between asymmetric

and symmetric states. In this sense, the change in the CRZ appearance in the present study is just another outcome of the interaction between CRZ and ISL.

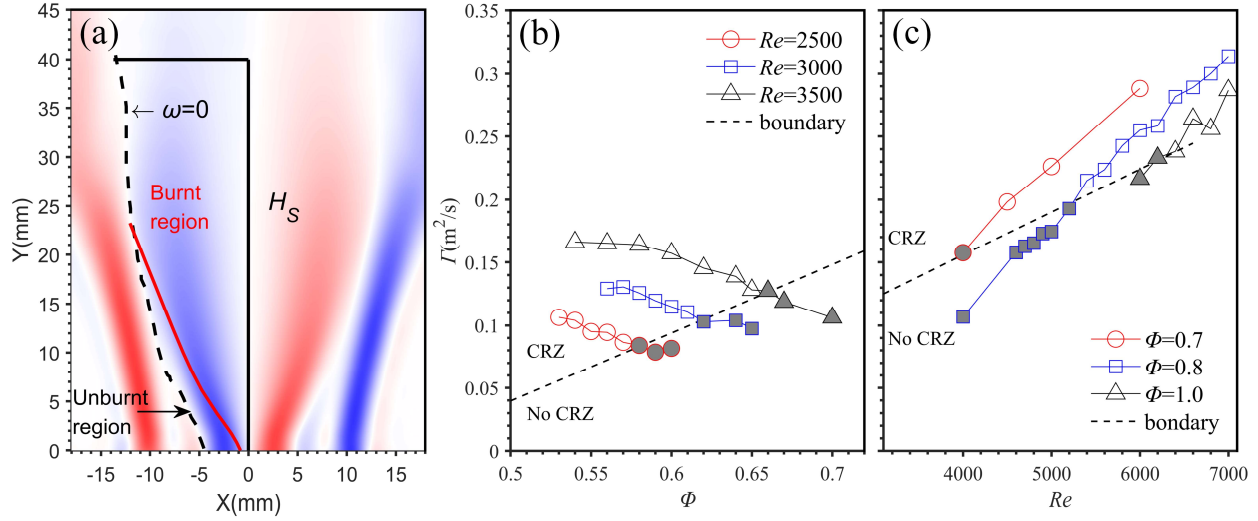


FIG. 9. Schematic showing the ISL region, encircled by the black lines, for circulation calculation; the red line represents the flame front which divides the ISL into a burnt and an unburnt region. (b) and (c) plot the circulation Γ as functions of Φ and Re , respectively, for different flames, with the dashed lines separating the cases with and without CRZ.

From the vortex-dynamics point of view, it happens as the vorticity in the ISL induces velocity opposite to the mainstream [27,28], promoting the formation and growth of CRZ. Here, circulation (Γ) is introduced as a measure for the total vorticity to quantify the strength of ISL, based on the area integration of the vorticity field in the form, $\Gamma = \iint \omega dA$. To determine the integration region A_s , the ISL boundary is first identified based on the zero-vorticity contour line and the y-axis, as illustrated in Fig.9(a). A_s should be sufficiently high to include the strong ISL in the near field and the CRZ for all cases. To find a proper height, we compared the ISL circulations with the heights of $H_s=40$ mm and 56 mm for different cases, and the differences were within 2.5%. So $H_s=40$ mm is sufficient for the calculations hereinafter. Note that the present work

considers only the overall average strength of the ISL based on the mean flow perspective, and it does not concern the dynamic process of vorticity growth in the shear layer contributed mainly by the effects of baroclinic torque and thermal expansion [29,30]. We do realize the importance of these mechanisms to the dynamical flame behaviors and will address them in a more relevant future study.

The circulation results for the same cases in Fig. 7 are plotted in Fig. 9(b) and 9(c), with the black-dashed line separating the cases with and without CRZ. We can observe that for a fixed Re in Fig. 9(b) the ISL circulation decreases with increasing Φ , while it increases with increasing Re for a constant Φ in Fig. 9(c). These trends of circulation variation agree with the dependence of the CRZ size on Re and Φ , as observed from Fig. 5 and Fig. 7, further verifying the correlation between the ISL intensity and the CRZ size. Furthermore, the results also demonstrate that the emergence of CRZ is constantly promoted by enhancing the circulation Γ when either Re or Φ is fixed. However, the critical Γ for a constant Re increases with Re and the critical Γ for a constant Φ increases with Φ , again implying that the emergence of the CRZ is not solely determined by the ISL intensity or Γ . Since the equivalence ratio Φ is also a relevant factor, we conjecture that there could be another mechanism through which the combustion reaction plays a role.

B. ISL-based mechanism for CRZ emergence

From the fluid mechanics perspective, the effect of the combustion reaction is generally twofold. One is the thermal expansion caused by the strong heat release from the reaction zone; its effect manifests in the significant flow acceleration, turning in the flow direction, as well as vorticity generation when the unburnt gas crosses the flame front. The other is related to the change of fluid properties, including gas density, viscosity, diffusivity, etc., owing to the increased temperature. The ISL circulation analyzed above has already accounted for the vorticity

contribution from thermal expansion, since it is essentially a time-averaged measure of all shearing effects, including the initial shear layer, vorticity generation, and vorticity dissipation. Therefore, the other mechanism affecting the CRZ characteristics and emergence could be related to the changed fluid properties.

Given the above analysis, we find in Fig. 5(a) that as the equivalence ratio increases and flame temperature rises, the ISL becomes weaker, and its vorticity seems to be more evenly distributed in the radial direction, which reflects an enhanced effect of viscous diffusion. This inspires us to correlate the other mechanism to the kinematic viscosity, which is strongly influenced by the gas temperature. Then, the higher critical Γ required for a higher Φ , as indicated from Fig. 9, can be explained as follows. In lean premixed flames, the high Φ causes a higher flame temperature which further leads to a higher viscosity; as such, the higher ISL strength is necessary to counter the faster rate of vorticity diffusion and annihilation at the center axis as well as the peripheral boundary. Following this understanding, the emergence of the CRZ in swirling flames is initiated by a sufficiently strong swirl, which induces vortex breakdown upstream and forms a strong ISL that feeds vorticity to maintain the CRZ. However, as the flame heats up the ISL and increases its viscosity, the vorticity in the ISL could diffuse rapidly to the axis and the surrounding OSL, where vorticity annihilation occurs; this could further lead to dissipation of the ISL and suppression of CRZ in the downstream. This mechanism is illustrated in Fig. 10. In this sense, the CRZ emergence is governed by a competition between the ISL strength, i.e., circulation, and the vorticity dissipation due to viscous diffusion, which can be characterized by a non-dimensional ratio,

$$Re_s = \frac{\Gamma}{\nu_s}, \quad (3)$$

where ν_s is the effective kinematic viscosity associated with the ISL. We denote this ratio Re_s as it has a form similar to the Reynolds number.

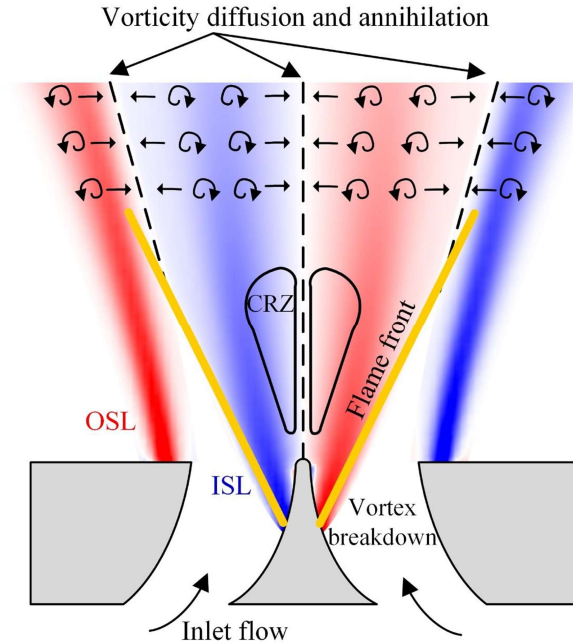


FIG. 10. The mechanisms governing the competition between CRZ emergence and suppression. The red and blue contours denote the vorticity distributions of positive and negative signs, respectively. The yellow lines are drawn to illustrate the flame front. The curled arrows represent the vorticity elements, and the straight arrow indicate the directions of vorticity diffusion.

C. The Re_s criterion

We next explore the validity of Re_s as a criterion for determining the CRZ emergence. To this end, the main challenge of calculating Eq. (3) lies in estimating the kinematic viscosity ν_s in the ISL, which is a function of the local gas temperature T [31]. Experimentally, it requires the application of non-intrusive temperature measurement, which is currently unavailable. Here, we propose a theoretical approximation of the actual temperature based on the adiabatic flame temperature (AFT). Since the ISL is divided by the flame front into an unburnt and a burnt part, as shown in Fig. 9(a), the temperature estimation should be performed for the two parts separately.

The temperature in the burnt region is considered to be the adiabatic flame temperature, whereas the temperature of the unburnt region is estimated using an interpolation scheme based on the particle concentration of the raw PIV images, similar to that reported by An *et al.* [32]. Consequently, an upper-limit estimation for ν_s can be obtained by area-weighted averaging the viscosities in the burnt and unburnt regions. The results for all cases are listed in Table. AI of the Appendix.

The resultant $\Gamma - \nu_s$ relation is plotted in Fig. 11, where the solid black line is a fitted boundary separating the cases with and without the CRZ. The boundary is roughly linear with its extension through the origin for the large-viscosity or large- Φ cases, suggesting that the emergence of the CRZ can be determined by a critical Re_s of 580 ± 15 . However, for the small-viscosity or small- Φ cases, the boundary line tends to intersect the x -axis; meanwhile, the critical Re_s for the emergence of the CRZ decreases with decreasing viscosity. The distinct behaviors between the large- Φ and small- Φ cases likely reflect the different accuracies in applying the AFT assumption for the ISL temperature estimation. For the large- Φ cases, massive heat release is produced compared with the heat loss to the environment so that the ISL temperature is relatively close to the AFT. However, for the small- Φ cases, the heat release is not sufficient to resist the heat loss, which causes the ISL temperature to drop substantially below the AFT, and further leads to significant overestimations of ν_s in the $\Gamma - \nu_s$ plot.

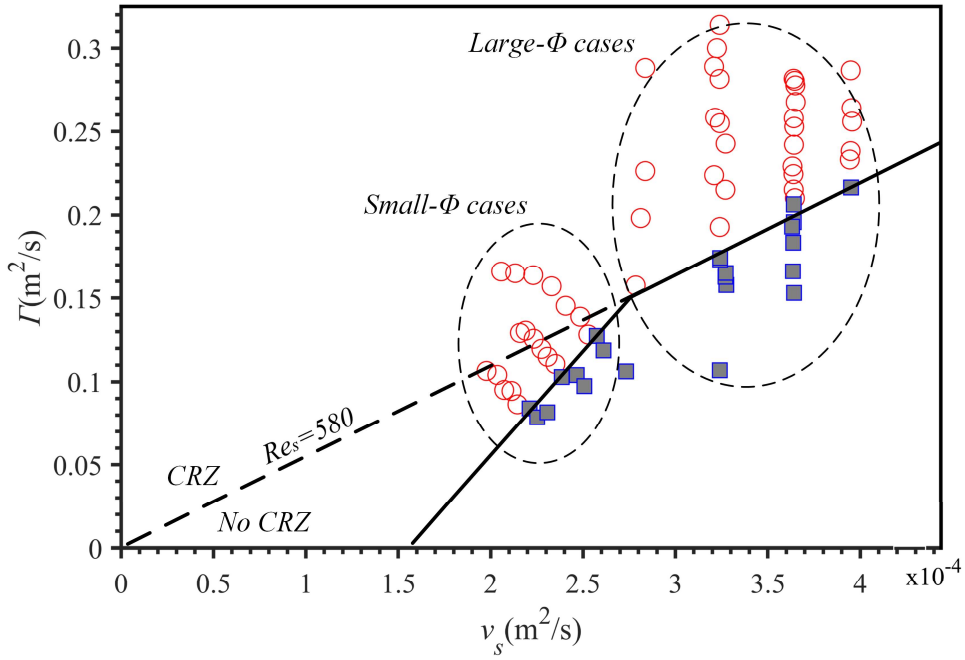


FIG. 11. Γ vs. ν_s for all cases in Fig. 4, with ν_s evaluated based on the adiabatic flame temperature. The large- Φ cases render a critical Re_s of 580 ± 15 .

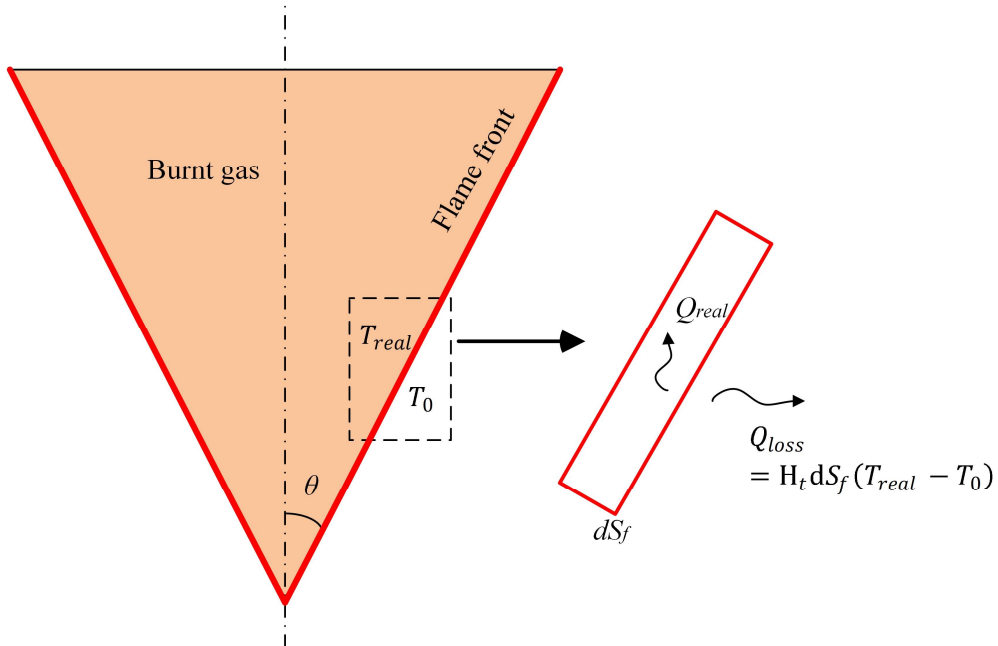


FIG. 12. A simple convective heat transfer model for the V-shaped unconfined flame front.

The above effect of Φ on the temperature of the burned gas in the ISL can be understood with a simple convective heat transfer model, which balances the heat release discrepancy at the flame front and the heat loss to the ambient air, as illustrated in Fig. 12. For ideal adiabatic combustion, the heat release Q_{ad} from a flame surface element dS_f can be calculated as

$$Q_{ad} = c_p \bar{m} dS_f (T_{ad} - T_0), \quad (4)$$

where T_{ad} is the adiabatic flame temperature, T_0 the temperature of the unburnt reactants, c_p the effective constant-pressure specific heat, and \bar{m} the mass flux of reactants crossing the flame surface. However, in reality, the temperature T_{real} of the burnt gas is lower than T_{ad} , corresponding to a net heat release of

$$Q_{real} = c_p \bar{m} dS_f (T_{real} - T_0). \quad (5)$$

For the present methane/air flame with a relatively small size, we may neglect the thermal radiation and attribute the heat loss entirely to convection. Thus, the heat loss Q_{loss} from the same flame surface element dS_f takes the form,

$$Q_{loss} = H_t dS_f (T_{real} - T_0), \quad (6)$$

where H_t is the effective convective heat transfer coefficient, and the ambient air temperature is considered to be T_0 as well. From the previous analysis, the difference between the adiabatic heat release and the actual heat release should equal the heat loss, expressed as $Q_{ad} - Q_{real} = Q_{loss}$, which can be combined with Eqs. (4), (5), and (6) to give

$$c_p \bar{m} (T_{ad} - T_{real}) = H_t (T_{real} - T_0), \quad (7)$$

where dS_f cancels on both sides. Recall the definition of the laminar flame speed S_L for premixed flame [33], $S_L = \frac{\bar{m}}{\rho_u}$, where ρ_u is the density of the unburnt reactants, Eq. (7) can be further derived

as

$$T_{ad} - T_{real} = \left(\frac{H_t}{H_t + c_p \rho_u S_L} \right) (T_{ad} - T_0). \quad (8)$$

Assuming H_t , c_p , and ρ_u to be constants, and T_{ad} and S_L are functions of the equivalence ratio Φ , we can normalize $(T_{ad} - T_{real})$ by its quantity at $\Phi = 1$ as

$$\Delta T_n = (T_{ad} - T_{real})_n = \left[\left(\frac{H_t}{H_t + c_p \rho_u S_L(\Phi)} \right) (T_{ad}(\Phi) - T_0) \right]_n. \quad (9)$$

Eq. (9) can be estimated based on the data of $T_{ad}(\Phi)$ and $S_L(\Phi)$ for methane/air flame [34] with known values of H_t , c_p , and ρ_u .

To have a first approximation for Eq. (9), ρ_u takes the density of air at 1atm and 300K, and c_p takes the corresponding value of air at 1atm and 1100K ($\approx 0.5(T_0 + T_{ad})$ at an equivalence ratio of 0.75 for methane/air flame). The estimation of H_t is more challenging since the actual flame temperature or the burned gas was not measured in the present work. Assuming flames of similar configuration and flow regime have comparable heat transfer characteristics, we can take advantage of the temperature data of two different V-shaped swirling flames (also fueled by premixed methane/air) reported in the literature [35,36] to compute their effective heat transfer coefficients with Eq. (8); the relevant parameters are listed in Table I, where T_{exp} is the averaged measured temperature of the CRZ. Note that, although the two flames were generated from different combustors and of distinct operating conditions (Re , Φ , S_N), the resulting H_t end up to be relatively close. Therefore, we consider the average H_t of these two flames, $0.037 \text{ kW}/(\text{m}^2\text{K})$, to be a reasonable approximation for the heat transfer coefficient in the simplified model of Eq. (8), as long as the flame is within the same regime. The resultant estimation of ΔT_n is plotted in Fig. 13, which shows that ΔT_n decreases with increasing Φ for lean combustion, verifying our previous conjecture that the ISL temperature is closer to the AFT when Φ is larger.

Table I. Parameters of two different flames in Ref. [35,36] for the estimation of H_t .

$No.$	Re	Φ	S_N	$T_0(K)$	$T_{ad}(K)$	$T_{exp}(K)$	$H_t(kW/m^2K)$
1	10000	0.83	0.75	300	2040	1880	0.0381
2	4900	0.8	0.6	300	1997	1817	0.0357

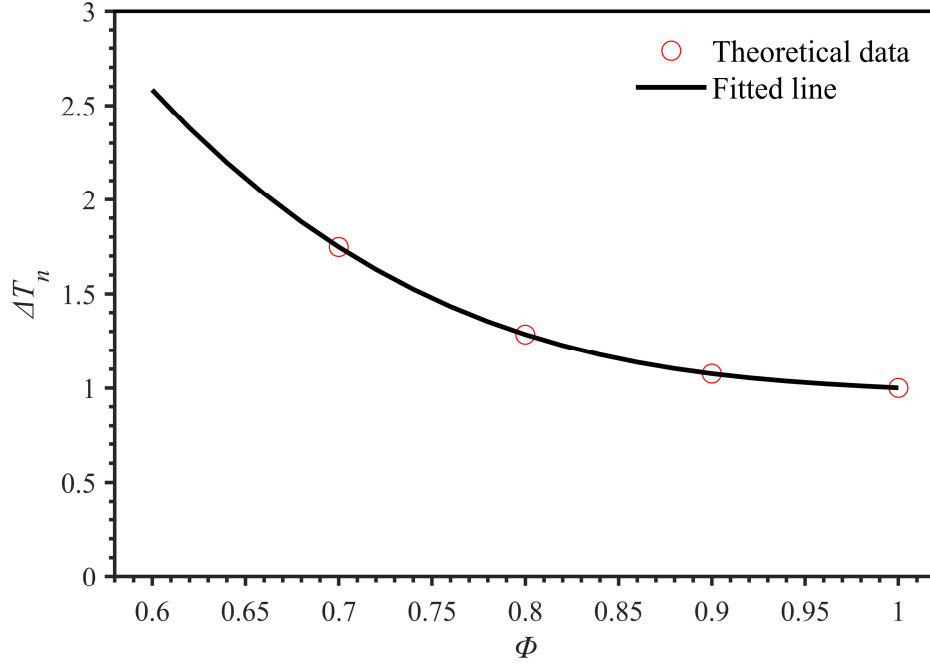


FIG. 13. Variation of ΔT_n with Φ calculated from Eq. (9), based on the methane/air flame data in the literature [34].

We next apply Eqs. (8) and (9) to obtain the adjusted flame temperature T_r and, consequently, the adjusted ISL viscosity ν_{sr} , as shown in Table. AI of the Appendix, yielding an adjusted $\Gamma - \nu_s$ diagram in Fig. 14. We see that a single linear boundary line through the origin exists between the regions with and without the CRZ; and the critical Re_s is determined to be 637 ± 21 based on the slope of this fitted line. The performance of the Re_s criterion in determining the CRZ emergence is significantly improved over that of Fig. 11, especially at the small- Φ end, justifying the ISL-dominated mechanism together with the heat loss correction.

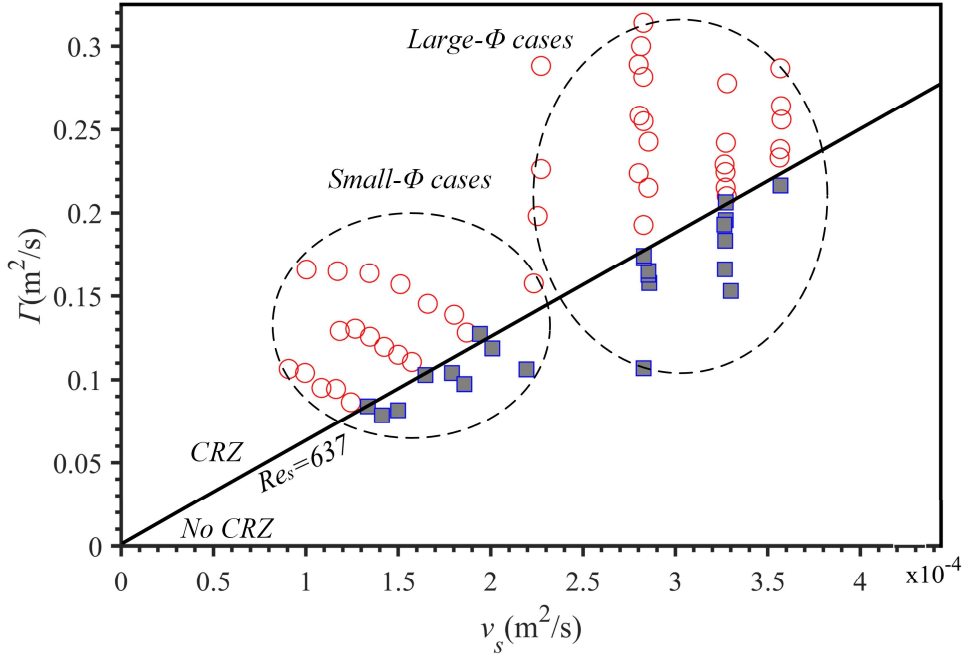


FIG. 14. The adjusted relation of Γ vs. v_s , with v_s evaluated based on the flame temperature calculated from Eq. (8). The boundary between CRZ and No CRZ collapses to a single line for both the small- and large- Φ cases, yielding a critical Re_s of 637 ± 21 .

Before closing, it should be mentioned that, while the present V-shaped flames belong to the low-swirl regime, the conclusions regarding the influences of the ISL on CRZ may be extended to the high-swirl cases with some modifications, as the underlying mechanism is similar. Specifically, an enhanced swirl intensity is likely to cause a larger flame angle and promote the formation tendency of the CRZ, which could be reflected in a different critical Re_s . In addition, the effect of a considerably increased Re of the premixed gas is also of interest, since the enhanced turbulent effective viscosity could play an essential role in governing the vorticity diffusion within the ISL. We can imagine that when Re is sufficiently large, the turbulent transport effect could become comparable with or even dominant over the molecular diffusion at high temperature. These topics are worth addressing in future works.

V. CONCLUDING REMARKS

In this paper, the emergence of the central recirculation zone (CRZ) in a V-shaped premixed swirling flame was experimentally investigated using a simultaneous measurement of PIV and CH* chemiluminescence. By tuning the Reynolds number Re and equivalence ratio Φ of the methane-air premixture, it was found that both increasing the Re and decreasing the Φ could facilitate the emergence of the CRZ. The effects of Re and Φ on CRZ were then analyzed based on the mean vorticity field. The strong correlation between the size of the CRZ and the strength of its surrounding inner shear layer (ISL) demonstrates an essential role of ISL in governing the characteristics of CRZ. Further quantitative analysis showed that the CRZ emergence can be promoted by enhancing the ISL intensity, in terms of circulation, at fixed Re or Φ .

Furthermore, the combustion reaction also plays an essential role by increasing the gas temperature in the ISL, thereby enhancing the viscous diffusion that could lead to strong vorticity dissipation and suppression of the CRZ. Accordingly, the emergence of CRZ can be understood as the outcome of a competition between the ISL intensity and the viscous-induced vorticity consumption, giving rise to the definition of a special Reynolds number, Re_s , based on the circulation and effective kinematic viscosity of the ISL. Re_s was then proposed as a criterion for deciding the CRZ emergence and validated against the present experimental data. Applying the adiabatic flame temperature (AFT) to approximate the ISL temperature, we showed that the large- Φ cases tend to share a common critical Re_s of around 580 for the CRZ emergence. However, for the small- Φ cases, the critical Re_s drops as the viscosity decreases. This deviation of small- Φ was attributed to a significantly overestimated viscosity, which is associated with the gap between the actual flame temperature and the AFT. Applying a simple heat loss model to correct this

temperature gap as well as its resulting discrepancy in the ISL viscosity, we were able to attain an adjusted critical Re_s of about 637, which is substantiated by both the small- and large- Φ data.

Last, the significance of the present work is emphasized. In general, the CRZ emergence in swirling flames can be explained from the point of vortex breakdown because it dictates the upstream onset of CRZ. The current result brings to our attention the overlooked role of strong viscous diffusion, as a result of flame heating, in reducing the ISL's strength, further leading to the size reduction or even suppression of the CRZ downstream.

ACKNOWLEDGMENTS

This work was supported partly by the National Natural Science Foundation of China (Grant No. 52006139, 92041001, and 12072194) and partly by the Shanghai Sailing Program (Grant No. 20YF1420600).

APPENDIX

This appendix reports additional information on the temperature and viscosity estimations of the ISL. The parameters used for or resulting from the ISL temperature and viscosity estimations are provided in Table. AI. A_u , T_u , and ν_u represent the area, temperature, and viscosity of the unburnt region in the ISL. A_b denotes the area of burnt region in the ISL. T_a and ν_a respectively represent the temperature and viscosity of the burnt region under the adiabatic assumption, with ν_s being the estimated effective viscosity of the ISL. T_r and ν_r respectively represent the adjusted temperature and viscosity of the burnt region that are computed based on Eq. (8), and ν_{sr} is the adjusted effective viscosity of the ISL.

From Table. AI, the area A_u of the unburnt region is much smaller than that of the burnt region A_b , and decreases with increasing Re . In addition, as Φ increases, the temperature T_a or T_r

in the burnt region increases and so does the viscosity ν_a or ν_r . Given the above observations, we reach a qualitative understanding that the effective viscosity of the ISL is dominated by the burnt region and should increase with Φ .

TABLE AI. Temperature and viscosity estimations of the ISL

<i>No.</i>	<i>Re</i>	Φ	A_u (mm^2)	A_b (mm^2)	T_u (<i>K</i>)	T_a (<i>K</i>)	T_r (<i>K</i>)	$\nu_u \cdot 10^6$ (m^2/s)	$\nu_a \cdot 10^6$ (m^2/s)	$\nu_r \cdot 10^6$ (m^2/s)	$\nu_s \cdot 10^6$ (m^2/s)	$\nu_{sr} \cdot 10^6$ (m^2/s)
1	2500	0.53	70	319	526	1537	1072	42	232	99	198	89
2	2500	0.54	66	323	517	1555	1109	41	237	109	204	98
3	2500	0.55	65	319	536	1574	1146	44	241	120	207	107
4	2500	0.56	65	315	526	1592	1182	42	246	130	211	115
5	2500	0.57	64	312	522	1611	1217	42	250	139	215	123
6	2500	0.58	62	323	535	1629	1251	43	255	149	221	132
7	2500	0.59	60	314	534	1647	1285	43	260	158	225	140
8	2500	0.60	57	322	531	1665	1317	43	264	167	231	148
9	3000	0.56	59	338	530	1592	1182	43	246	130	216	117
10	3000	0.57	61	345	545	1611	1217	45	250	139	219	126
11	3000	0.58	60	338	541	1629	1251	44	255	149	223	134
12	3000	0.59	59	333	538	1647	1285	44	260	158	228	141
13	3000	0.60	59	335	535	1665	1317	43	264	167	231	148
14	3000	0.61	59	332	533	1683	1349	43	269	176	235	155
15	3000	0.62	60	338	533	1701	1381	43	273	184	239	164
16	3000	0.64	57	328	545	1736	1440	45	282	202	247	178
17	3000	0.65	60	334	573	1753	1469	49	287	209	251	185
18	3500	0.54	63	329	524	1555	1109	42	237	111	206	99
19	3500	0.56	64	334	525	1592	1182	42	246	130	213	116
20	3500	0.58	60	342	529	1629	1251	43	255	149	223	133
21	3500	0.60	55	338	533	1665	1317	43	264	167	233	149
22	3500	0.62	55	340	525	1701	1381	42	273	184	241	165

23	3500	0.64	56	345	534	1736	1440	43	282	201	249	179
24	3500	0.65	56	346	538	1753	1469	44	287	208	253	186
25	3500	0.66	56	341	556	1771	1498	46	292	216	258	193
26	3500	0.67	54	334	566	1788	1525	48	296	224	261	200
27	3500	0.70	54	332	575	1838	1603	49	310	245	273	219
28	4000	0.70	49	356	570	1838	1603	48	310	245	279	222
29	4500	0.70	43	352	578	1838	1603	49	310	245	281	225
30	5000	0.70	41	366	566	1838	1603	48	310	245	284	226
31	6000	0.70	39	354	567	1838	1603	48	310	245	284	226
32	4000	0.80	37	336	623	1997	1824	56	354	306	324	282
33	4600	0.80	35	360	619	1997	1824	55	354	306	328	285
34	4700	0.80	35	353	624	1997	1824	56	354	306	327	284
35	4800	0.80	34	349	612	1997	1824	54	354	306	327	285
36	4900	0.80	40	359	632	1997	1824	57	354	306	324	281
37	5000	0.80	39	347	629	1997	1824	57	354	306	324	281
38	5200	0.80	39	351	619	1997	1824	55	354	306	324	281
39	5400	0.80	35	351	624	1997	1824	56	354	306	327	281
40	5600	0.80	43	344	613	1997	1824	54	354	306	321	279
41	5800	0.80	34	344	630	1997	1824	57	354	306	327	285
42	6000	0.80	39	349	621	1997	1824	55	354	306	324	282
43	6200	0.80	44	360	610	1997	1824	54	354	306	322	280
44	6400	0.80	40	360	611	1997	1824	54	354	306	324	282
45	6600	0.80	43	351	612	1997	1824	54	354	306	321	279
46	6800	0.80	42	358	615	1997	1824	55	354	306	323	281
47	7000	0.80	40	358	616	1997	1824	55	354	306	324	282
48	5000	0.90	35	355	683	2134	1999	65	394	354	364	329
49	5200	0.90	36	355	682	2134	1989	65	394	352	364	326
50	5400	0.90	36	362	674	2134	1989	63	394	352	364	326
51	5600	0.90	35	356	677	2134	1989	64	394	352	364	326

52	5800	0.90	35	337	679	2134	1989	64	394	352	363	326
53	5900	0.90	34	343	668	2134	1989	62	394	352	364	326
54	6000	0.90	34	350	690	2134	1989	66	394	352	365	326
55	6100	0.90	35	349	667	2134	1989	62	394	352	364	326
56	6200	0.90	36	351	665	2134	1989	62	394	352	363	326
57	6300	0.90	35	351	680	2134	1989	64	394	352	364	326
58	6400	0.90	35	351	676	2134	1989	64	394	352	364	326
59	6500	0.90	35	358	683	2134	1989	65	394	352	365	327
60	6600	0.90	33	338	686	2134	1989	65	394	352	364	327
61	6700	0.90	33	350	673	2134	1989	63	394	352	365	327
62	6800	0.90	35	356	668	2134	1989	62	394	352	364	326
63	6900	0.90	34	346	664	2134	1989	62	394	352	364	326
64	7000	0.90	35	359	682	2134	1989	65	394	352	365	327
65	6000	1.00	31	360	746	2226	2091	75	423	380	395	356
66	6200	1.00	31	346	752	2226	2091	76	423	380	395	355
67	6400	1.00	30	344	732	2226	2091	72	423	380	395	356
68	6600	1.00	30	354	741	2226	2091	74	423	380	395	356
69	6800	1.00	30	352	739	2226	2091	73	423	380	396	357
70	7000	1.00	32	363	735	2226	2091	73	423	380	395	356

-
- [1] P. Weigand, W. Meier, X. R. Duan, W. Stricker, and M. Aigner, Investigations of swirl flames in a gas turbine model combustor: I. Flow field, structures, temperature, and species distributions, *Combustion and flame* **144**, 205 (2006).
- [2] Y. Liu, X. Sun, V. Sethi, D. Nalianda, Y. Li, and L. Wang, Review of modern low emissions combustion technologies for aero gas turbine engines, *Progress in Aerospace Sciences* **94**, 12 (2017).
- [3] G. Bulat, E. Fedina, C. Fureby, W. Meier, and U. Stopper, Reacting flow in an industrial gas turbine combustor: LES and experimental analysis, *Proceedings of the Combustion Institute* **35**, 3175 (2015).
- [4] O. Lucca-Negro and T. O'doherty, Vortex breakdown: a review, *Progress in energy and combustion science* **27**, 431 (2001).
- [5] N. Syred and J. M. Beér, Combustion in swirling flows: a review, *Combustion and flame* **23**, 143 (1974).
- [6] P. Anacleto, E. Fernandes, M. Heitor, and S. Shtork, Swirl flow structure and flame characteristics in a model lean premixed combustor, *Combustion Science and Technology* **175**, 1369 (2003).
- [7] T. B. Benjamin, Theory of the vortex breakdown phenomenon, *Journal of Fluid Mechanics* **14**, 593 (1962).
- [8] T. Sarpkaya, Vortex breakdown in swirling conical flows, *AIAA journal* **9**, 1792 (1971).
- [9] K. J. Nogenmyr, H. J. Cao, C. K. Chan, and R. K. Cheng, Effects of confinement on premixed turbulent swirling flame using large Eddy simulation, *Combustion Theory and Modelling* **17**, 1003 (2013).
- [10] Y. Wang, X. Wang, and V. Yang, Evolution and transition mechanisms of internal swirling flows with tangential entry, *Physics of Fluids* **30**, 013601 (2018).
- [11] F. C. Gouldin, J. S. Depsky, and S. L. Lee, Velocity field characteristics of a swirling flow combustor, *AIAA journal* **23**, 95 (1985).
- [12] J. Choi, Z. Rusak, and A. Kapila, Numerical simulation of premixed chemical reactions with swirl, *Combustion theory and modelling* **11**, 863 (2007).
- [13] C. O. Umeh, Z. Rusak, and E. Gutmark, Vortex breakdown in a swirl-stabilized combustor, *Journal of Propulsion and Power* **28**, 1037 (2012).
- [14] G. Wang, X. Liu, X. Xia, S. Wang, and F. Qi, Dynamics of periodically-excited vortices in swirling flames, *Proceedings of the Combustion Institute* **38**, 6183 (2021).
- [15] S. Wang, J. Zheng, L. Li, Z. Yang, X. Xia, C. Fu, Y. Gao, X. Liu, X. Han, and C. Zhang, Evolution characteristics of 3D vortex structures in stratified swirling flames studied by dual-plane stereoscopic PIV, *Combustion and Flame* **237**, 111874 (2022).
- [16] S. Wang, J. Zheng, L. Xu, Q. An, X. Han, C. Zhang, L. Li, X. Xia, and F. Qi, Experimental investigation of the helical mode in a stratified swirling flame, *Combustion and Flame* **244**, 112268 (2022).

- [17] A. Valera-Medina, N. Syred, P. Kay, and A. Griffiths, Central recirculation zone analysis in an unconfined tangential swirl burner with varying degrees of premixing, *Experiments in Fluids* **50**, 1611 (2011).
- [18] C. J. Dasch, One-dimensional tomography: a comparison of Abel, onion-peeling, and filtered backprojection methods, *Applied optics* **31**, 1146 (1992).
- [19] Y. Huang and V. Yang, Effect of swirl on combustion dynamics in a lean-premixed swirl-stabilized combustor, *Proceedings of the Combustion Institute* **30**, 1775 (2005).
- [20] M. S. Sweeney, S. Hochgreb, M. J. Dunn, and R. S. Barlow, The structure of turbulent stratified and premixed methane/air flames II: Swirling flows, *Combustion and Flame* **159**, 2912 (2012).
- [21] W. Liu, R. Xue, L. Zhang, Q. Yang, and H. Wang, Dynamic Response of a Forced Low-Swirl Premixed Flame with Acoustic Excitation, *Flow, Turbulence and Combustion* **108**, 1139 (2022).
- [22] P. Palies, D. Durox, T. Schuller, and S. Candel, The combined dynamics of swirler and turbulent premixed swirling flames, *Combustion and flame* **157**, 1698 (2010).
- [23] J. O'Connor and T. Liewen, Recirculation zone dynamics of a transversely excited swirl flow and flame, *Physics of fluids* **24**, 2893 (2012).
- [24] N. A. Chigier and J. M. Beér, Velocity and Static-Pressure Distributions in Swirling Air Jets Issuing From Annular and Divergent Nozzles, *Journal of Basic Engineering* **86**, 788 (1964).
- [25] M. Stöhr, I. Boxx, C. D. Carter, and W. Meier, Experimental study of vortex-flame interaction in a gas turbine model combustor, *Combustion and flame* **159**, 2636 (2012).
- [26] R. Zhang, I. Boxx, W. Meier, and C. D. Slabaugh, Coupled interactions of a helical precessing vortex core and the central recirculation bubble in a swirl flame at elevated power density, *Combustion and Flame* **202**, 119 (2019).
- [27] G. L. Brown and J. M. Lopez, Axisymmetric vortex breakdown Part 2. Physical mechanisms, *Journal of Fluid Mechanics* **221**, 553 (1990).
- [28] M. Kröner, J. Fritz, and T. Sattelmayer, Flashback Limits for Combustion Induced Vortex Breakdown in a Swirl Burner, *Journal of Engineering for Gas Turbines and Power* **125**, 693 (2003).
- [29] P. A. McMurtry, J. J. Riley, and R. W. Metcalfe, Effects of heat release on the large-scale structure in turbulent mixing layers, *Journal of Fluid Mechanics* **199**, 297 (1989).
- [30] A. Kazbekov, K. Kumashiro, and A. M. Steinberg, Enstrophy transport in swirl combustion, *Journal of Fluid Mechanics* **876**, 715 (2019).
- [31] J. A. van Oijen, Flamelet-generated manifolds: development and application to premixed laminar flames, Ph.D. thesis, Eindhoven University Press, 2002.
- [32] Q. An, W. Y. Kwong, B. D. Geraedts, and A. M. Steinberg, Coupled dynamics of lift-off and precessing vortex core formation in swirl flames, *Combustion and Flame* **168**, 228 (2016).
- [33] R. T. Stephen, *An introduction to combustion: concepts and applications*, (McGrw-Hill Companies, Inc, 2000).
- [34] C. K. Law, *Combustion physics*, (Cambridge university press, 2010).
- [35] M. A. Gregor, F. Seffrin, F. Fuest, D. Geyer, and A. Dreizler, Multi-scalar measurements in a premixed swirl burner using 1D Raman/Rayleigh scattering, *Proceedings of the Combustion Institute* **32**, 1739 (2009).

- [36] X. Liu, G. Wang, J. Zheng, L. Xu, S. Wang, L. Li, and F. Qi, Temporally resolved two dimensional temperature field of acoustically excited swirling flames measured by mid-infrared direct absorption spectroscopy, *Optics Express* **26**, 31983 (2018).